RSC Advances

ROYAL SOCIETY OF CHEMISTRY

www.rsc.org/advances

A Highly-Ordered and Uniform Sunflower-like Dendritic Silver Nanocomplex Array as Reproducible SERS Substrate

Jian Chu,[a] Yue Zhao,[a] Shu-Hong Li,[a] Wen-Wei Li,[a] Xiang-Yu Chen,[c] Yu-Xi Huang,[a] You-Peng Chen,[a] Wen-Gang Qu,[b] Han-Qing Yu,*[a] An-Wu Xu,[b] Gang Liu,[c] Yang-Chao Tian,[c] Ying Xiong[c]

Surface-enhanced Raman scattering (SERS) is widely recognized as a powerful analytical tool. However, its application has been limited by the lack of reliable and reproducible metal-particle substrate. In this work, a silver (Ag) nanocomplex array SERS substrate with highly-ordered and uniform sunflower-like structure was fabricated by integrating the deep-ultraviolet lithography and electrodepositon methods. The as-prepared nanocomplex array, consisting of a thin circular Ag nanoparticle layer in the centre and dendritic Ag nanostructures at the flange, exhibited a substantial enhancement in Raman signals and good reproducibility for SERS measurement of 4-aminothiophenol. The dendritic nanostructures were formed as a result of the edge effect and diffusion-limited aggregation. The morphology and Raman signal enhancement of the substrate were governed by electrodepositon parameters such as electrodepositon time, deposition potential and citric acid concentration. This fabrication approach is facile, cost-effective, highly reproducible and easily controllable, offering a great opportunity for large-scale production of substrate and practical application of SERS.

Introduction

Surface-enhanced Raman scattering (SERS) is a powerful analytical tool to be widely used in the fields of chemistry[1-3], biology[4, 5], medicine[6, 7], environment[8, 9] and national defense[10-12]. In SERS, the Raman enhancement is mostly attributed to a plasmon excitation through electromagnetic enhancement mechanism[13, 14], which results in hot spots around nano-sized metal particles of the substrate. Thus, the performance of this technology relies heavily on the use of reliable and reproducible substrate with uniform metal nanoparticles, which has become a severe constraint for its application so far[15]. Conventional methods for SERS substrate fabrication mostly adopt roughened electrodes[1] or gold/silver colloidal suspensions[16]. In addition, several lithographic techniques, including electron beam lithography (EBL)[17, 18] and interference lithography (IL)[19], have also been used to produce more uniform and tunable nanoparticle substrates. However, these techniques generally need costly instrumentation and suffer from low throughput rates or small overall writing areas[19].

Deep-ultraviolet (DUV) contact lithography is recognized as a simple and cost-effective approach for nanomaterial fabrication, but it is not directly applicable for the fabrication of metal nanostructure with 'hot spots' due to its limited resolution[20]. On the other hands, electroless deposition[21-24] and electrochemical deposition[25-27] has been widely used to synthesize noble metal nanoparticles onto substrates. This method offers excellent control over the particle size and shape, but does not allow for lateral organization into a regular array[28].

[a] *CAS Key Laboratory of Urban Pollutant Conversion, Department of Chemistry, University of Science and Technology of China, Hefei, 230026, China E-mail: hqyu@ustc.edu.cn*
[b] *Division of Nanomaterials and Chemistry, Hefei National Laboratory for Physical Sciences at Microscale, University of Science and Technology of China, Hefei, 230026, China*
[c] *National Synchrotron Radiation Laboratory, University of Science and Technology of China, Hefei, 230026, China*
Electronic supplementary information (ESI) available: Figs.S1–S5. See DOI:

Considering the advantages and disadvantages of both methods, we propose that a combined use of the DUV contact lithography and electrochemical deposition may enable the fabrication of more tunable substrate with better process controllability and reproducibility than the above approach alone, although more steps were needed than the one-step chemical reduction for preparation of Au/Ag colloidal suspensions. More specifically, a regular and well-designed photoresist pattern was fabricated on electrode using a simple DUV lithography process. Then, the photoresist pattern was directly used as a template for electrochemical deposition of dendritic silver nanostructure. With this photoresist template, the dendritic silver nanostructure was constrained to form sunflower-like dendritic silver nanocomplex array with uniform size and morphology.

Therefore, in this study, we explored the feasibility of using this integrated method for SERS substrate fabrication. A highly-ordered, uniform dendritic silver nanocomplex array with sunflower-like structure was fabricated, and exhibited good performance as SERS substrate for measurement of 4-aminothiophenol (4-ATP). Also, the changes of substrate morphology and Raman enhancement effect are examined.

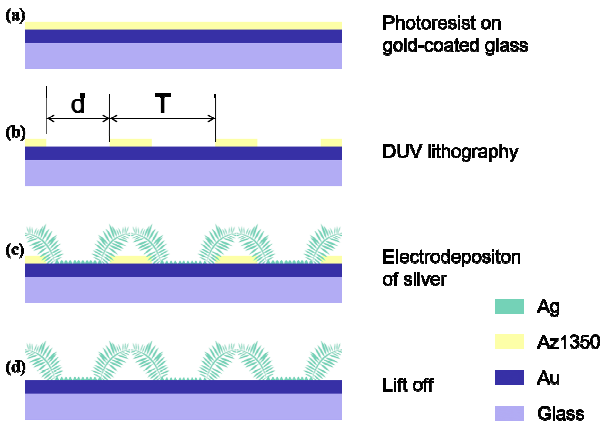

Scheme 1 Fabrication process of the Ag nanocomplex array on gold-coated glass. (a) a layer of AZ1350 positive photoresist (600-nm thick) is spin-coated onto the gold

layer; (b) Periodic hole array pattern of photoresist is fabricated by DUV lithography (d is the hole diameter and T is period of the pattern); (c) Electrodepositon of Ag nanocomplex; and (d) After the electrodepositon, the photoresist is lift off with isopropanol and rinsed thoroughly

Experimental Section

Preparation of Ag nanostructures on gold-coated glass

Prior to Ag electrodepositon, a glass substrate (60 × 60 × 2 mm) was washed with detergent and rinsed with deionized water and acetone in sequence. The glass substrate was then sputter deposited with a thin layer of chromium and Au layer of about 100-nm thickness, serving as the conducting layer of the electrode for the subsequent electrodepositon. After that, a highly ordered hole array photoresist pattern was fabricated on the electrode using a ultraviolet photolithography method, i.e., spin-coating a layer of 600-nm thick AZ1350 positive photoresist onto the Au layer (**Scheme 1**a). Following soft-bake at 100 °C for 10 min, the positive photoresist on the substrate was exposed to a photomask containing the hole array pattern of the metal tracks (exposure: g-line, 30 mJ/cm^2; development: 0.6% NaOH, 1 min) (**Scheme 1**b). After development, the remaining photoresist was cleaned with oxygen plasma (30 W, ME-3A MEIRE, Institute of Microelectronics, China) for 30 s to obtain a Au electrode with a hole array template on the surface. The electrodeposition was performed in a two-electrode cell connected to a electrochemical workstation (CHI 842b, CH Instruments Inc., USA). The typical electroplating solution consisted of 1 g of citric acid, 0.1 g of Ag nitrate and 100 mL H_2O. Pre-cutting to the appropriate size (~1 cm in width) of the Au electrode with the photoresist hole array template, the working electrode, was used as the cathode, and a titanium plate (40 mm × 60 mm) as the anode. The distance between the two electrodes was about 1 cm. The electrodepositon potential (E) was held at -2.4 V for 20 s. The electrodepositon process was carried out at ambient temperature (~20 °C). After the electrodepositon, the photoresist holes were filled with Ag nanostructure (**Scheme 1**c). Then, the photoresist template was removed using isopropanol, followed by rinsing with acetone and deionized water. After deep cleaning in saturated NaOH aqueous solution at 70 °C for 1 h, Ag nanostructures was formed on the gold layer, and used as SERS substrate (**Scheme 1**d).

Characterization of the Ag nanocomplex

The Ag nanocomplex array was characterized using X-ray photoelectron spectroscopy (XPS) (ESCALAB 250, Thermo-VG Scientific Co., USA), scanning electron microscopy (SEM) (e-Line, Raith Co., Germany), high resolution transmission electron microscopy (HRTEM), selected area electron diffraction (SAED) (JEM 2010, JEOL Co., Japan) and ultraviolet-visible-near-infrared diffuse reflectance spectroscopy (UV-Vis-NIR DRS) (SOLID 3700, Shimadzu Co., Japan).

SERS and Raman mapping measurements

The SERS performance of the substrate was evaluated by using 4-ATP as the probe analyte. To examine the detection limit of 4-ATP, Ag nanostructures formed in same condition (E = -2.4 V, concentration of citric acid = 10 g/L) were immersed in 4 mL of 4-ATP ethanol solutions with various of concentrations (1×10^{-9} M, 1×10^{-8} M, 1×10^{-7} M, 1×10^{-6} M and 1×10^{-5} M) over night. To explore the impacts of the fabrication parameters (e.g., concentration of citric acid and deposition potential), the Ag nanostructures formed in different conditions were all immersed in 4 mL 4-ATP ethanol solutions (1×10^{-5} M) over night. Before Raman measurements, these Ag nanostructures were dried in air and rinsed with ethanol. To evaluate its enhancement factor, 2 μL of 4-ATP aqueous solution (1×10^{-5} M and 1×10^{-6} M) was dropped onto the spots with the Ag nanostructures, while 2 μL of 4-ATP aqueous solution (1×10^{-3} M) was dropped onto a bare gold-coated glass as a comparison. The SERS spectra were measured under ambient temperature using confocal micro-Raman spectroscopy (LABRAM-HR, JY Co., France). A semiconductor laser with 785-nm radiation was used as the excitation source. The laser beam was focused by a 100 × microscope objective (N.A. = 0.9), resulting in a spot of around 1 μm in diameter. The laser power on the samples was ca. 2~3 mW. The data acquisition time for collection of each spectrum was 2 s. The spectrometer was calibrated using the Raman band of a silicon wafer at 520 cm^{-1}. To simplify the calculation, the peak intensity of Raman spectrum is calculated as follows: Intensity (1076 cm^{-1}) = Value (1076 cm^{-1}) – Value (1050 cm^{-1}); Intensity (1143 cm^{-1}) = Value (1143 cm^{-1}) – Value (1100 cm^{-1}). In Raman mapping measurements, a 50 × long working distance microscope objective (N.A. = 0.5) was used, and all the spectra were baseline corrected by the NGS-LabSpec^{TM} on the instrument. The mosaic images were drawn through a home-made program with Matlab^{TM}.

Result and discussion

The fabrication process of the Ag nanocomplex array on gold-coated glass is schematically illustrated in **Scheme 1**. The SEM image in **Fig. 1**a reveals that highly ordered Ag arrays were electrodeposited on the pre-patterned photoresist template. The morphology of the synthesized Ag nanocomplex array varied with the electrodeposition time (**Fig. 1**b). Specifically, a thin film of Ag nanoparticles was deposited inside the circular hole confined by photoresist template, while the edge of the nanocomplex was composed of dendritic Ag nanostructure. A closer view (insert in **Fig. 1**a) clearly reveals the presence of tree branch-like nanocrystals with a width of 30-50 nm and many interparticle gaps, possibly resulting in an electromagnetic enhancement of the substrate under visible laser illumination. In addition, the formed Ag nanocomplexes were uniform over a large area (insert in **Fig. S2**), which provides a foundation for a uniform Raman enhancement.

The XPS spectrum of the substrate is illustrated in Supplementary **Fig. S1**. Peaks of Ag $3d_{5/2}$ (368.35 eV) and Ag $3d_{3/2}$ (374.4 eV) can be clearly observed in the high-resolution spectra (insert in **Fig. S1**), suggesting the presence of Ag(0)[29, 30]. The Au peaks can be attributed to the Au layer on glass substrate. The UV-Vis-NIR DRS spectrum of the Ag nanocomplex on gold film shows a plasmon absorption peak at 381 nm (**Fig. S2**). In addition, the TEM, HRTEM and SAED images reveal that Ag dendrite nanostructure at the edge of the Ag nanocomplex was composed of bunches of Ag nanocrystals (**Fig. S3**).

In a typical electrodepositon process, Ag nanoparticles were initially nucleated inside the photoresist hole (**Fig. 1**b, Phase I), where the conductive Au layer was exposed. Then, in the reaction process, the Ag^+ concentration nearby the electrode decreased rapidly with concomitant generation of depositing current (**Fig. 1**b, Phase II). However, the depositing current increased a little at the later stage of deposition (**Fig. 1**b, Phase III). This should be

attributed to the diffusion and deposition of Ag^+ ions from the bulk solution and the formation of dendritic Ag nanostructures at the edge of the photoresist hole, which increased the effective surface area of the electrode. Eventually, most Ag^+ ions were deposited to form dendritic Ag nanostructures at the hole edge, while only the initial thin Ag nanopartide film remained in the hole. After photoresist template was removed by solvents, an ordered and uniform Ag nanocomplex array with sunflower-like structure was obtained.

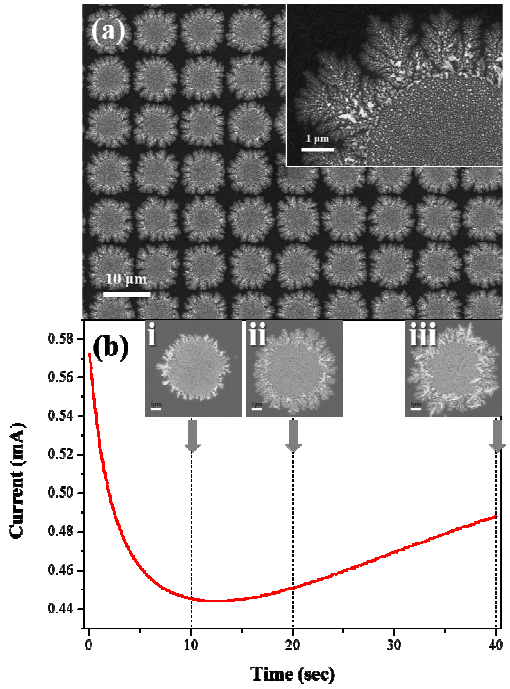

Fig. 1 (a): SEM image of the Ag nanocomplex array. Insert shows a closer view of the dendritic Ag nanostructure at the edge of the photoresist hole. (b): Chronocoulometry cure for electrodepositing process. Inset SEM images show the Ag nanostructures from different deposition times. The scale bar is 1 μm

As shown in **Fig. 1**a insert, the Ag nanocomplex was constructed by a thin layer of Ag nanoparticles in the center and dense dendritic Ag nanostructures at the edge. The comparison of the Raman intensities between the two different parts shows that the dendritic Ag structure exhibited a much stronger Raman intensity, about 10 times larger than the center part (**Fig. S4**). Previous studies have demonstrated that Raman signal enhancement is mainly attributed to electromagnetic field enhancement, which creates hot spots around metal nanoparticles[11]. Thus, nanoscale gaps (hot spots) and sharp tips in metal nanostructures are essential to enable the features to produce the Raman scattering enhancement[31]. Here, the Ag dendrite nanostructure at the flange (The TEM image is shown in **Fig. S3**a) was the main contributor to the electromagnetic field enhancement. Therefore, in the subsequent tests, the SERS data were all collected at the border of the Ag nanocomplex, unless otherwise specified.

The enhanced Raman spectra (on Ag nanocomplex) and the conventional Raman spectrum (on flat Au film) of 4-ATP are shown in **Fig. 2**a. The peak intensities of 4-ATP on the Ag nanocomplex were dramatically enhanced compared to that on the flat Au film. Vibrational assignments of the five strongest peaks are shown in **Table 1**. It should be mentioned that conclusive assignments of the so-call "b_2 modes" of 4-ATP, including the bands at *ca.* 1143, 1386, 1432 cm^{-1}, are still controversial[32-35]. These b_2 modes were interpreted as charge transfer (CT) modes for 4-ATP in some report[32, 35], while Huang et al.[33, 34] pointed out that the "b_2 mode" bands were originated from 4-dimercaptoazobenzne (DMAB), an oxidative coupling product of 4-ATP produced during Raman measurement. To avoid confusion, the subsequent discussion was mainly based on the "a_1 mode" at *ca.* 1076 cm^{-1}. From the peak intensity located at 1076 cm^{-1}, the EF (Raman enhancement factor) was calculated to be ~1.16×10^5.

Table 1 Vibrational Assignments of Raman Spectrum

Wavenumber (cm^{-1})	Assignments	
	4-ATP[32]	DMAB[34]
1076	ν_{CS}	
1143		ν_{CN}
1386		ν_{NN}
1432		ν_{NN}
1571	ν_{CC}	ν_{CC}

Fig. 2b shows a typical SERS spectra of 4-ATP with concentrations ranging from 10^{-9} to 10^{-5} M adsorbed on the Ag nanocomplex array. At low concentrations (about ≤ 10^{-6} M), only the strongest peak at 1076 cm^{-1} could be recognized. A positive correlation between peak intensity and 4-ATP concentration was observed.

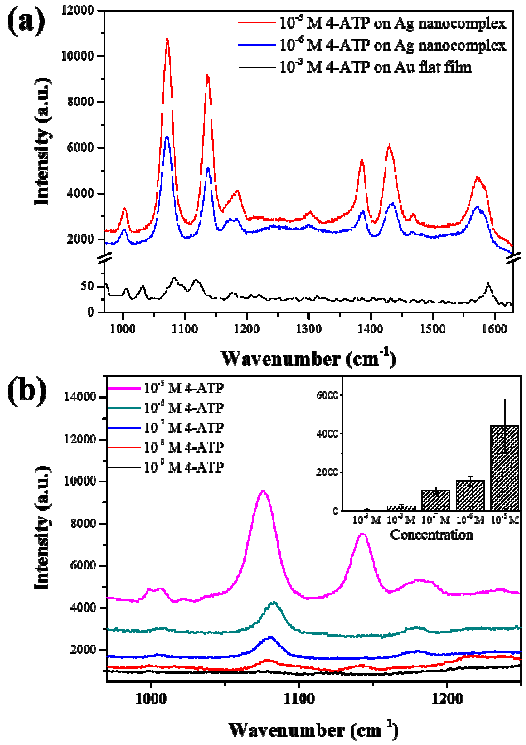

Fig. 2 (a): Raman spectra of 4-ATP with various concentrations adsorbed on Ag nanocomplex array. Insert shows the peak intensity at 1076 cm^{-1} increased with the concentration of 4-ATP; (b) Comparison between Raman spectra of 4-ATP dropped on Ag nanocomplex and flat Au film.

To evaluate the reproducibility of the Ag nanocomplex array for SERS measurement, the SERS spectra of 4-ATP, collected from 10 random points of two independent substrates, were compared. As shown in **Fig. 3**a, the peak intensities at *ca.*1076 cm^{-1} of these spectra from the ten points were very close to each other. For the peaks at ~1076 cm^{-1}, the relative standard deviation (RSD) of the measured SERS intensities of two independent substrates were both approximately 8 %, and the deviation between these two samples was about 7.1 % (**Fig. 3**b), demonstrating a very good reproducibility of the as-prepared SERS substrate.

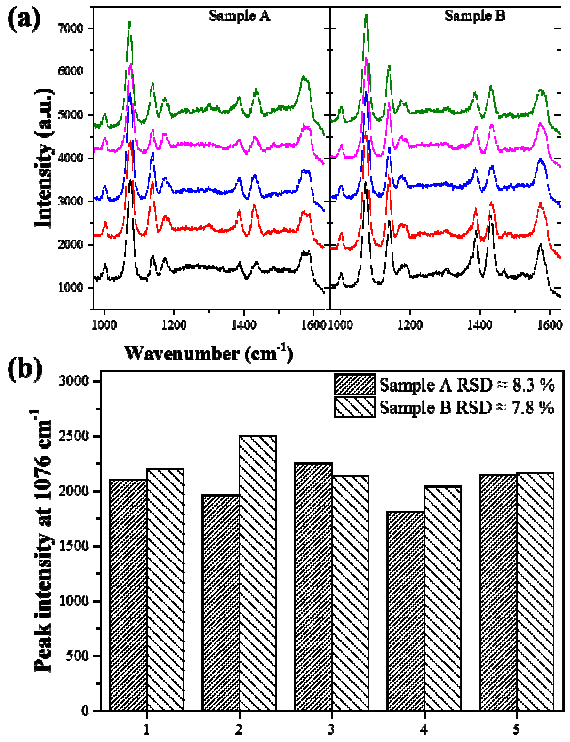

Fig. 3 (a) SERS spectra of 1×10^{-5} M 4-ATP on 10 random points of two independent Ag nanocomplex arrays. Laser: 785 nm, 2 mW; Objective lens: 100× / 0.9; and integration time: 2 s; (b) Peaks intensity at ~1076 cm^{-1} distribution of 4-ATP obtained from 10 random sites on the Ag nanocomplex and the calculated RSD.

In electroplating solution, citric acid, which served as a chelating ligand for Ag^+ ion, would reduce Ag^+ concentration and slow down the deposition of Ag nanoparticles. When electrodepositon process began in the absence of citric acid, the surface Ag^+ concentration on the gold film decreased rapidly. Due to the concentration polarization, only a thin film consisting of small-sized Ag nanoparticles was formed in the circular hole, as shown in **Fig. 1**b, Phase I. Then, Ag^+ ions in the bulk solution diffuses and tiny Ag nanoparticles became deposited at the edge of the circular Ag film, forming branch-like structures (**Fig. 4**a). When citric acid was induced, both Ag^+ activity and the deposition rate of Ag nanoparticles further reduced. The slower deposition rate would result in a larger particle size (**Fig. 4**b-d)[36]. As shown in **Fig. 4**f, compared to the Ag nanocomplex deposited in pure $AgNO_3$ aqueous solution, the presence of a certain amount of citric acid promoted the formation of larger Ag dendritic nanostructure, which could further enhance the Raman signals of 4-ATP. However, a too high concentration of citric acid (e.g., above 20 g/L) was detrimental to the formation of Ag dendritic nanostructure. Therefore, in this study, 5~10 g/L was chosen as the appropriate citric acid concentration.

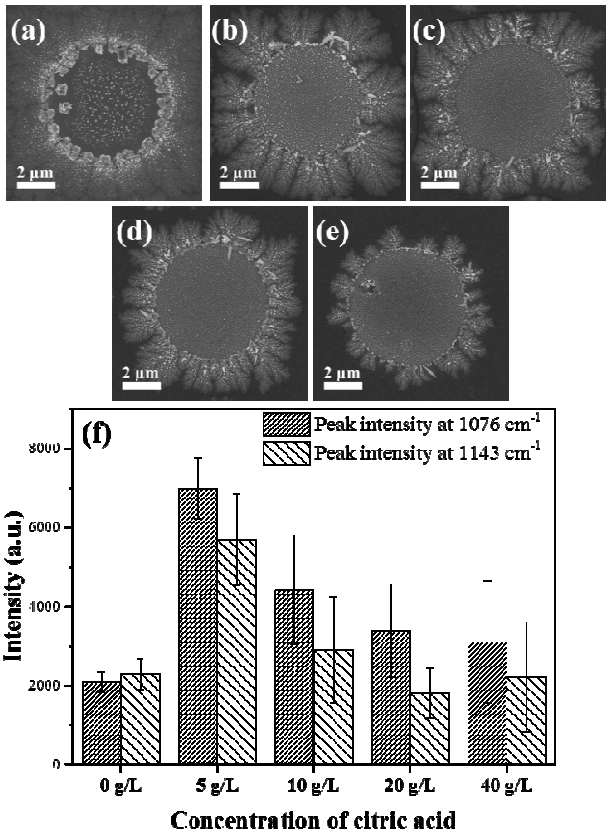

Fig. 4 (a-e): SEM images of the Ag nanocomplex deposited with different concentrations of citric acid: (a) 0 g/L; (b) 5 g/L; (c) 10 g/L; (d) 20 g/L; and (e) 40 g/L. The scale bar is 2 μm. (g): Peaks intensity (at ~1143 cm^{-1} and ~1076 cm^{-1}) of 1×10^{-5} M 4-ATP on the Ag nanocomplexes deposited in different concentrations of citric acid. NAZ: Ag nanoparticles deposited in 10 g/L citric acid without pre-patterned photoresist template

In electrochemical systems, the deposition rate affects the morphology of formed nanostructures. Since the deposition rate can be controlled by adjusting the overpotential[37], application of a suitable potential is thus of crucial importance. The synthesis of Ag nanocomplex under different deposition potentials, from -1.2 V to -3.0 V, was investigated. **Fig. 5**a-d shows that, under a low potential of -1.2 V, no dendritic nanostructures were formed, and only a dense layer of Ag film was developed in the hole defined by the photoresist template. Accordingly, no significant Raman enhancement was observed (**Fig. 5**f). When applying a more negative potential of -1.8 V, Ag nanocomplex with sparse dendritic nanostructures was obtained. The most intensive dendritic nanostructures were obtained at the most negative potential, -3.0 V under the tested conditions, as well as the Raman intensity of 4-ATP on these nanostructures. Consistent with common sense, the denser dendritic nanostructures can provide more adsorption sites and Raman hot spots, both of which are beneficial to Raman enhancement.

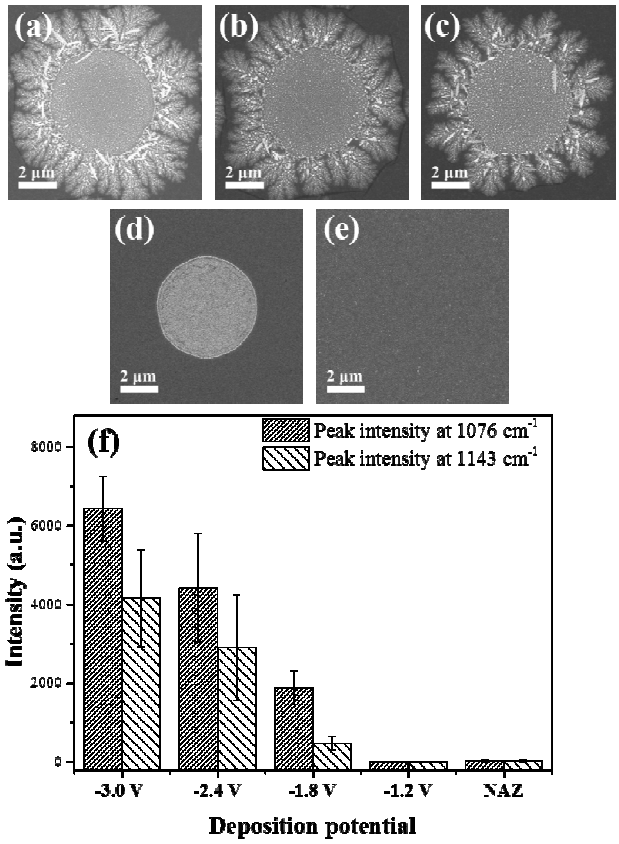

Fig. 5 (a-e): SEM images of the Ag nanocomplex deposited under different deposition potentials for 20 s: (a) -3.0V; (b) -2.4 V; (c) -1.8 V; (d) -1.2 V. and (e) -2.4 V but without photoresist templates. The scale bar is 2 μm. (f): Peak intensity (at ~1143 cm^{-1} and ~1076 cm^{-1}) of 1×10^{-5} M 4-ATP on the Ag nanocomplexes deposited under different deposition potentials for 20 s.

However, only the negative potential is not sufficient to form the ordered dendritic nanostructures. As shown in **Fig. 5**e, without the photoresist templates on the Au layer, only a flat Ag film was obtained on substrate, even the potential was as negative as -2.4 V. No significant enhancement of Raman signal was observed in this case.

The side view SEM images of the photoresist template on Au layer before and after deposition are shown in **Fig. S5**a-b. Obviously, after the deposition, a large number of Ag branches grew along the sidewalls of the holes and spread above the photoresist, forming the edge of the nanocomplex, which had a main contribution to the adsorption and Raman signal enhancement. For a sparser photoresist pattern (T = 30 μm, d = 26 μm) (**Fig. S5**e, f), the Ag branches also grew along the sidewalls of the photoresist, regardless of the array shape (**Fig. S5**c, d). These results suggest that the Ag branch-nanostructure preferentially deposited at the boundary between the exposed conductive Au layer and the region covered by the insulated photoresist, and grew towards the insulated photoresist.

To further clarify the consistency of enhancement and applicability of the Ag nanocomplex array in routine Raman measurement, a Raman mapping was performed on a Ag nanocomplex array, with 10^{-5} M 4-ATP ethanol solution adsorbed (in **Fig. 6**). The whole mapping area was 60 × 60 μm. The step length was 10 μm, the same as the period of Ag nanocomplex, which ensures that every single spectrum was collected at a similar part of each Ag nanocomplex. The mosaic images show the intensity distributions of the five strongest peaks (**Fig. 6**b-f). The "a_1 modes" at *ca.* 1076 and 1571 cm^{-1}, which are clearly ascribed to 4-ATP, had a very small RSD in intensity distributions (both were about 6 %) on the whole test area. This measurement clearly indicates that the as-prepared Ag nanocomplex array exhibited a consistent Raman enhancement effect and was very convenient to obtain reproducible SERS signal in routine Raman measurement. In contrast, the relatively poor reproducible of the "b_2 modes" at *ca.* 1143, 1386 and 1432 cm^{-1}, with about 12 % RSD, implies a complicated origin of these bands as mentioned in Ref. 33.

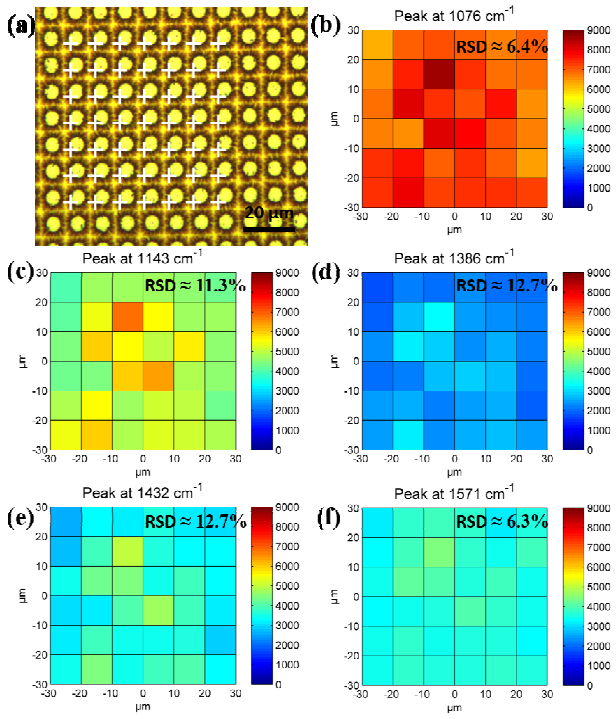

Fig. 6 Raman mapping of the Ag nanocomplex array. (a): Image of Ag nanocomplex array by optical microscope and indicator points for spectra acquisition, the scale bar is 20 μm; (b-f): The mosaic images of intensity distributions at the five strongest peaks and the corresponding RSD on the test area

In order to explain the unique morphology and formation process, a Ag nanocomplex growth mechanism is proposed and illustrated in **Scheme 2**. The current density and electric field strength distribution near the Au layer with / without photoresist template were simulated using COMSOL Multiphysics software (**Scheme 2**a). Under a certain potential, both the current density and electric field strength on the bare Au layer as well as the migration and nucleation of Ag^+ ion were uniform, leaving a flat Ag film on the Au layer (**Scheme 2**a upside). However, the existence of insulated photoresist on the Au layer drastically distorted the distributions of the current density and electric field strength near the electrode (**Scheme 2**a underside). Thereby, the migration and nucleation of Ag^+ ion became consistent with the pattern of the photoresist template. The Ag^+ ions on the Au layer surface nucleated on the electrode and formed a thin layer of Ag nanoparticles; then Ag^+ diffused from bulk solution rapidly and grew on the previously formed particles. If sufficient potential was applied to the electrode, the strongest current density and electric field would appear nearby the sidewalls of photoresist, where the subsequent majority of Ag^+

ion would migrate to and nucleate. Since the migration path of Ag^+ ion was similar with the current density, a three-dimensional diffusion occurred at the sidewalls of the photoresist hole[27] (**Scheme 2**b underside), and a sunflower-like Ag nanocomplex was formed on the electrode (**Fig. 4**a). When citric acid was added into the solution, the nucleation and growth process would be inhibited until a higher degree of supersaturation was achieved, and relatively sparse but thick dendritic nanostructures were obtained at the edge of photoresist hole (**Scheme 2**b underside). Thus, both the sufficient applied potential and photoresist templates on the Au layer were essential for the formation of the dendritic Ag nanocomplex, and the dose of citric acid could change their morphologies. These could be well explained by the diffusion-limited aggregation theory[38, 39].

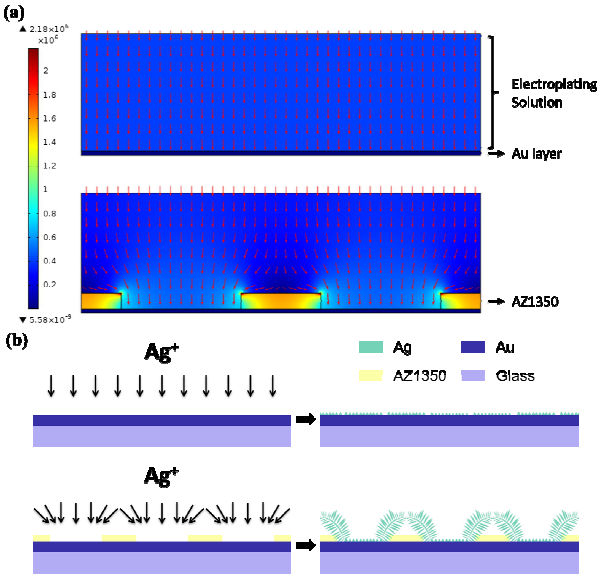

Scheme 2 (a) A 2-D finite element model of current density (arrow) and electric field strength (color map) distribution on electrodes with/without photoresist template. (b) Schematic diagram of diffusion of Ag^+ ion above the Au film with/without the pre-patterned photoresist template

Conclusions

In this work, we demonstrate that integration of DUV lithography method with electrodeposition offers a facile, cost-effective and reproducible approach for the fabrication of SERS substrate. With this approach, a highly-ordered and uniform sunflower-like dendritic Ag nanocomplex array with a large area, well-defined morphology and good Raman signal enhancement could be fabricated. The large-scale and cost-effective production of such SERS substrates thus greatly increases the possibility of practical SERS applications. In addition, the substrate morphology and Raman enhancement effect are found to be governed by the electrodepositon time, deposition potential and citric acid concentration, which implies a possibility of tuning the morphology of the Ag nanocomplex. Although the enhancement factor of the substrate fabricated by this method at the present stage might not be as high as some of those obtained by other methods, the low cost, great repeatability, high convenience and good controllability of the preparation process would provide sufficient justifications and momentum for its further development. Benefited from the progress of lithography techniques, more refined patterns and the development of nanostructure arrays with various types of metal (e.g., Au, Pt, Cu, and Au/Ag alloy, etc.) can be expected, which may ultimately make total analysis system with SERS substrate a real possibility. Therefore, this work adds to the potential of SERS substrate and is expected to accelerate the pace of development of next-generation SERS devices. Furthermore, this integrated approach may offer a versatile tool in preparing nanocomplexes for photonic crystals, photovoltaic conversion, electrochemical/chemical catalysis, and micro-electro mechanical system applications.

Acknowledgements

This work was supported by the National Basic Research Program of China (2011CB933702) and the Program for Changjiang Scholars and Innovative Research Team in University of China and and the Collaborative Innovation Center of Suzhou Nano Science and Technology of the Ministry of Education of China.

References

1. E. Cortes, P. G. Etchegoin, E. C. Le Ru, A. Fainstein, M. E. Vela and R. C. Salvarezza, *J. Am. Chem. Soc.*, 2010, **132**, 18034-18037.
2. G. S. Hu, Z. H. Feng, D. F. Han, J. Li, G. Q. Jia, J. Y. Shi and C. Li, *J. Phys. Chem. C*, 2007, **111**, 8632-8637.
3. G. S. Hu, Z. C. Feng, J. Li, G. Q. Jia, D. F. Han, Z. M. Liu and C. Li, *J. Phys. Chem. C*, 2007, **111**, 11267-11274.
4. S. E. Bohndiek, A. Wagadarikar, C. L. Zavaleta, D. Van de Sompel, E. Garai, J. V. Jokerst, S. Yazdanfar and S. S. Gambhir, *Proc. Nat. Acad. Sci. U. S. A.*, 2013, **110**, 12408-12413.
5. J. D. Driskell, K. M. Kwarta, R. J. Lipert, M. D. Porter, J. D. Neill and J. F. Ridpath, *Anal. Chem.*, 2005, **77**, 6147-6154.
6. F. Domenici, A. R. Bizzarri and S. Cannistraro, *Anal. Biochem.*, 2012, **421**, 9-15.
7. C. M. MacLaughlin, E. P. Parker, G. C. Walker and C. Wang, *Nanomed. Nanotechnol. Biol. Med.*, 2013, **9**, 55-64.
8. B. Liu, G. Han, Z. Zhang, R. Liu, C. Jiang, S. Wang and M. Y. Han, *Anal. Chem.*, 2012, **84**, 255-261.
9. J. F. Li, Y. F. Huang, Y. Ding, Z. L. Yang, S. B. Li, X. S. Zhou, F. R. Fan, W. Zhang, Z. Y. Zhou, Y. Wu de, B. Ren, Z. L. Wang and Z. Q. Tian, *Nature*, 2010, **464**, 392-395.
10. L. Yang, L. Ma, G. Chen, J. Liu and Z. Q. Tian, *Chem. Eur. J.*, 2010, **16**, 12683-12693.
11. H. Zhou, Z. Zhang, C. Jiang, G. Guan, K. Zhang, Q. Mei, R. Liu and S. Wang, *Anal. Chem.*, 2011, **83**, 6913-6917.
12. M. S. Schmidt, N. Kostesha, F. Bosco, J. K. Olsen, C. Johnsen, K. A. Nielsen, J. O. Jeppesen, T. S. Alstrom, J. Larsen, T. Thundat, M. H. Jakobsen and A. Boisen, *Micro- and Nanotechnology Sensors, Systems, and Applications Iii*, 2011, **8031**.
13. L. Qin, S. Zou, C. Xue, A. Atkinson, G. C. Schatz and C. A. Mirkin, *Proc. Nat. Acad. Sci. U. S. A.*, 2006, **103**, 13300-13303.
14. M. L. Pedano, S. Li, G. C. Schatz and C. A. Mirkin, *Angew. Chem. Int. Ed.*, 2010, **49**, 78-82.
15. X. M. Lin, Y. Cui, Y. H. Xu, B. Ren and Z. Q. Tian, *Anal. Bioanal. Chem.*, 2009, **394**, 1729-1745.
16. W. E. Doering and S. M. Nie, *J. Phys. Chem. B*, 2002, **106**, 311-317.
17. L. Gunnarsson, E. J. Bjerneld, H. Xu, S. Petronis, B. Kasemo and M. Käll, *Appl. Phys. Lett.*, 2001, **78**, 802.

18. M. Sackmann, S. Bom, T. Balster and A. Materny, *J. Raman Spectrosc.*, 2007, **38**, 277-282.
19. P. K. Sahoo, K. Vogelsang, H. Schift and H. H. Solak, *Appl. Surf. Sci.*, 2009, **256**, 431-434.
20. J. G. Goodberlet, *Appl. Phys. Lett.*, 2000, **76**, 667.
21. S. Wang and H. Xin, *J. Phys. Chem. B*, 2000, **104**, 5681-5685.
22. K. G. M. Laurier, M. Poets, F. Vermoortele, G. D. Cremer, J. A. Martens, H. Uji-i, D. E. De Vos, J. Hofkens and M. B. J. Roeffaers, *Chem. Commun.*, 2012, **48**, 1559-1561.
23. A. Gutés, C. Carraro and R. Maboudian, *J. Am. Chem. Soc.*, 2010, **132**, 1476-1477.
24. A. Gutés, R. Maboudian and C. Carraro, *Langmuir*, 2012, **28**, 17846-17850.
25. X. Qin, Z. Y. Miao, Y. X. Fang, D. Zhang, J. Ma, L. Zhang, Q. Chen and X. G. Shao, *Langmuir*, 2012, **28**, 5218-5226.
26. S. Q. Wang, L. P. Xu, Y. Q. Wen, H. W. Du, S. T. Wang and X. J. Zhang, *Nanoscale*, 2013, **5**, 4284-4290.
27. Y. P. Chen, Y. Zhao, K. Q. Qiu, J. Chu, H. Q. Yu, G. Liu, Y. C. Tian and Y. Xiong, *Electrochim. Acta*, 2011, **56**, 9088-9094.
28. L. A. Dick, A. D. McFarland, C. L. Haynes and R. P. Van Duyne, *J. Phys. Chem. B*, 2002, **106**, 853-860.
29. J. Bearden and A. Burr, *Rev. Mod. Phys.*, 1967, **39**, 125-142.
30. J. C. Fuggle and N. Martensson, *J. Electron. Spectrosc. Relat. Phenom.*, 1980, **21**, 275-281.
31. N. G. Greeneltch, M. G. Blaber, A. I. Henry, G. C. Schatz and R. P. Van Duyne, *Anal. Chem.*, 2013, **85**, 2297-2303.
32. M. Osawa, N. Matsuda, K. Yoshii and I. Uchida, *J. Phys. Chem.*, 1994, **98**, 12702-12707.
33. Y. F. Huang, D. Y. Wu, H. P. Zhu, L. B. Zhao, G. K. Liu, B. Ren and Z. Q. Tian, *PCCP*, 2012, **14**, 8485-8497.
34. Y. F. Huang, H. P. Zhu, G. K. Liu, D. Y. Wu, B. Ren and Z. Q. Tian, *J. Am. Chem. Soc.*, 2010, **132**, 9244-9246.
35. D. P. Fromm, A. Sundaramurthy, A. Kinkhabwala, P. J. Schuck, G. S. Kino and W. E. Moerner, *J. Chem. Phys.*, 2006, **124**, 4.
36. C. M. McShane and K. S. Choi, *J. Am. Chem. Soc.*, 2009, **131**, 2561-2569.
37. C. D. Gu and T. Y. Zhang, *Langmuir*, 2008, **24**, 12010-12016.
38. T. Witten and L. Sander, *Phys. Rev. Lett.*, 1981, **47**, 1400-1403.
39. R. Ball, M. Nauenberg and T. Witten, *Phys. Rev. A*, 1984, **29**, 2017-2020.

Table of Contents

A highly reproducible SERS substrate of Ag nanocomplex array with highly-ordered sunflower-like structure has been fabricated by integrating lithography and electrodepositon.